TABLE I Atomic positions for the planar defect compared to those for the non-defective infinite-layer unit cell

Planar defect atomic positions				Corresponding non-defective infinite-layer atomic positions			
Atom	x	y	z	Atom	x	y	z
Cu	0	0	0	Cu	0	0	0
O(1)	0.5	0	0	O	0.5	0	0
O(1)	0	0.5	0	O	0	0.5	0
O(2)*	0	0	0.29	O†	–	–	–
O(2)*	0	0	0.71	O†	–	–	–
				O	0.5	0	0.5
O(3)	0.5	0.5	0.5				
				O	0	0.5	0.5
Sr(1)*	0	0	0.422				
				Cu	0	0	0.5
Sr(1)*	0	0	0.578				
Sr(2)	0.5	0.5	0.20	Sr	0.5	0.5	0.25
Sr(2)	0.5	0.5	0.80	Sr	0.5	0.5	0.75

The unit cell for the defect is $3.9 \times 3.9 \times 7.4$ Å (x, y, z), while that for the non-defective infinite-layer compound is: $3.9 \times 3.9 \times 6.8$ Å (x, y, (2)z). The atomic positions are scaled to the unit-cell length. The staggering of Sr(1) is 0.078 times the unit-cell length along c-axis, which results in Sr(1) positions being, $0.50 - 0.078 = 0.422$ and $0.50 + 0.078 = 0.578$.

* Half occupancy.

† No apical oxygens.

CuO_2 and Sr–O layers, allowing new structures to form. The triple Sr–O layer model can than be thought of as an extension of the double Sr layers present in $Sr_{n+1}Cu_nO_{2n+1+x}$ compounds. We have not seen any defects with more than three layers in these compounds. While other known hole-doped copper oxide superconductors have a homogeneous occupancy of apical oxygen sites there are no apical oxygen atoms in the non-defective infinite-layer compound. It appears that the planar defects provide at least half of the possible number of the apical oxygens to the CuO_2 planes and therefore permit hole-doped high-T_c superconductivity. (The previously proposed[10] half-occupancy of apical oxygen sites in Sr_2CuO_3 has been called into question by recent neutron-diffraction experiments.[11])

It should be pointed out that neither X-ray microanalysis nor HREM imaging can define the oxygen content and locations precisely. The two Sr positions (both Sr(1) and Sr(2)) are determined here with a high degree of confidence, but the O positions are assigned according to the cation positions. Because the cation position is dictated by anion coordination, the observed staggering of Sr(1) is clearly due to the reduction of apical oxygen occupancy, which is also consistent with the charge neutrality arguments.

We speculate that these planar defects can be p-type if doped by excess oxygen ($x > 0$) or n-type with oxygen deficiency ($x < 0$), leading to both p- and n-type superconductivity. Furthermore, for $x = 0$, one can obtain neutral Sr_3O_2 layers. This hypothesis agrees with previous observations of superconductivity in this system[4] as a function of the synthesis atmosphere, that is p-type with $T_c \approx 110$ K under oxidizing conditions and n-type with $T_c \approx 43$ K under reducing conditions.

We have found that compositions with excess cation ($y > 1$) show an increased Meissner fraction by a factor of almost four, relative to the stoichiometric or $y < 1$ compositions. This is consistent with A-cation-rich planar defects observed in this study. In our most recent experiments on pure $SrCuO_2$ (that is, no calcium), we also observe planar defects similar to those reported here and they too are Sr-rich. □

Received 8 April; accepted 28 June 1994.

1. Siegrist, T., Zahurak, S. M., Murphy, D. W. & Roth, R. S. *Nature* **334,** 231–232 (1988).
2. Azuma, M., Hiroi, Z., Takano, M., Bando, Y. & Takeda, Y. *Nature* **356,** 775–776 (1992).
3. Jorgensen, J. D., Radaelli, P. G., Hinks, D. G. & Wagner, J. L. *Phys. Rev.* B**47,** 14654–14656 (1993).
4. Hiroi, Z., Azuma, M., Takano, M. & Takeda, Y. *Physica* C**208,** 286–196 (1993).
5. Adachi, S., Yamauchi, H., Tanaka, S. & Mori, N. *Physica* C**208,** 226–230 (1993).
6. Radaelli, P. G. & Jorgensen, J. D. *Nature* **364,** 286–287 (1993).
7. Dravid, V. P., Zhang, H., Zhang, J. P. & Marks, L. D. *Physica* C**192,** 31–34 (1992).
8. Principles of Analytical Electron Microscopy (eds Joy, D. C., Romig, A. Jr & Goldstein, J. I.) Ch. 4 & 5 (Plenum, New York, 1986).
9. Adachi, S., Yamauchi, H., Tanaka, S. & Mori, N. *Physica* C**212,** 164–168 (1993).
10. Hiroi, Z., Azuma, M., Takano, M. & Takeda, Y. *Nature* **364,** 315–317 (1993).
11. Shimakawa, Y. *et al. Physica* C. (in the press).

ACKNOWLEDGEMENTS. The research was supported by the NSF US through the Science and Technology Center for Superconductivity (STCS) and the US Department of Energy.

Light-emitting diodes made from cadmium selenide nanocrystals and a semiconducting polymer

V. L. Colvin, M. C. Schlamp & A. P. Alivisatos

Materials Sciences Division, Lawrence Berkeley Laboratory, and Department of Chemistry, University of California at Berkeley, Berkeley, California 94720, USA

ELECTROLUMINESCENT devices have been developed recently that are based on new materials such as porous silicon[1] and semiconducting polymers[2,3]. By taking advantage of developments in the preparation and characterization of direct-gap semiconductor nanocrystals[4–6], and of electroluminescent polymers[7], we have now constructed a hybrid organic/inorganic electroluminescent device. Light emission arises from the recombination of holes injected into a layer of semiconducting *p*-paraphenylene vinylene (PPV)[8–10] with electrons injected into a multilayer film of cadmium selenide nanocrystals. Close matching of the emitting layer of nanocrystals with the work function of the metal contact leads to an operating voltage[11] of only 4 V. At low voltages emission from the CdSe layer occurs. Because of the quantum size effect[19–24] the colour of this emission can be varied from red to yellow by changing the nanocrystal size. At higher voltages green emission from the polymer layer predominates. Thus this device has a degree of voltage tunability of colour.

Nanocrystals normally exist as powders or dissolved in liquids. To employ them in devices it is necessary to develop new techniques of assembly which allow charge injection into, and transport through, nanocrystals. To achieve this goal we construct multilayers of nanocrystals using the well-developed chemistry of thiols on metal surfaces. Narrow size distributions (±5% of the diameter) of CdSe nanocrystals with absorption maxima in the range 580–620 nm (30–50 Å diameter) are prepared by the TOPO method of Murray and Bawendi[5] as modified by Bowen Katari *et al.*[6]. The nanocrystals are dissolved in toluene, and this solution is exposed to either bare indium tin oxide (ITO) or ITO/PPV plates which have been pretreated with hexane dithiol, a bifunctional compound that binds nanocrystals to surfaces[6,12]. This procedure is repeated five times, leading to the formation of a multilayer structure with closely packed disordered sheets of CdSe nanocrystals separated by organic spacers. This well-characterized buildup process permits the isolated nanocrystals to be investigated before being incorporated into the diode structure. In addition, this process permits nanocrystals with different electronic properties to be placed in defined locations in the same device. The overall thickness of the nanocrystal multilayer is only a few hundred ångströms. This thin layer readily undergoes dielectric breakdown at the voltages required for operation. For this reason, a 1,000-Å-thick layer of PPV, prepared by standard methods (250 °C conversion temperature and absorption maximum at 415 nm), is a desirable

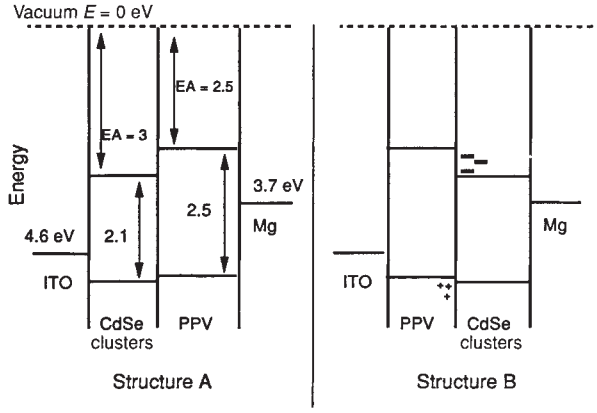

FIG. 1 Energy-level diagram for the composite samples. The work functions of indium tin oxide (ITO) (4.6 eV) and Mg (3.7 eV)[25] were provided by the literature; an upper limit for the electron affinity (EA) of PPV (2.5 eV) is assumed[16]. The band gaps of the CdSe nanocrystals and PPV are respectively 2.1 eV and 2.5 eV. The electron affinities of different sized CdSe nanocrystals are not known; we estimate a value averaged over many sizes based on the ionization potentials as measured by valence band photoemission[26]. In structure A the nanocrystals are closest to the ITO and, as can be seen from the Figure, neither the electrons or the holes are confined by the heterojunction. In the opposite arrangement (structure B), the higher electron affinity of CdSe leads to a lower operating voltage, as well as charge confinement at the heterojunction.

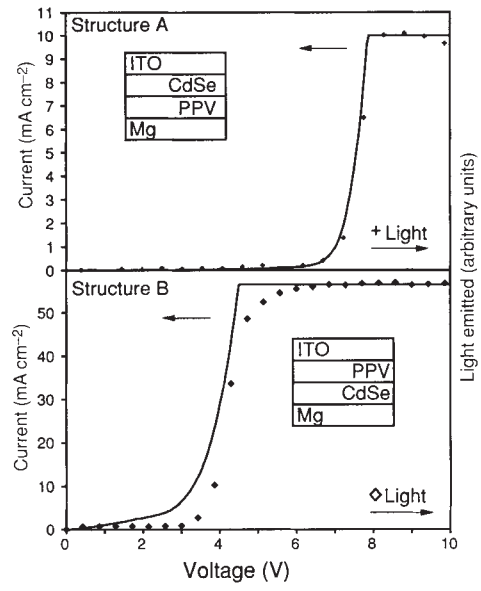

FIG. 2 Electrical characteristics of PPV/CdSe samples. As in plain PPV devices, the current–voltage (I/V) behaviour (solid line) of these devices is similar to that of a classic diode. The barrier to charge injection (and thus the barrier controlling our I/V curves) occurs at a metal/semiconductor junction and thus can be classified as a Schottky barrier. The points (+, ◇) show light intensity versus voltage for structures A and B. In structure A (top), the turn-on voltage is nearly 7 V (7×10^4 V cm^{-1}), and typical operating currents are 10 mA cm^{-2}. The plateau in the signal is the result of current limiting of the device to avoid shorting, and it is apparent that at this constant current value the emission intensity begins to fall with time under bias. In contrast, the light from structure B (bottom) is relatively stable over time, and the typical operating currents are much higher (50 mA cm^{-2}) with a luminance of 100 cd m^{-2}. Also, the operating voltage is much lower—which is to be expected if the electron affinity of the CdSe multilayer is greater than that of PPV. Under reverse bias, samples experience dielectric breakdown and no electroluminescent light is visible.

component of the sample. It both ensures electrical stability and enhances carrier injection and confinement. Figure 1 shows an energy-level diagram for two geometries, A and B. Electrical contact is made by magnesium coated with silver; X-ray photoemission studies of these contacts indicate that the magnesium is oxidized readily in air.

When subjected to a forward bias, with ITO positively biased with respect to magnesium, both of the sample geometries (Fig. 1) emit with a luminosity of ~100 cd m^{-2} (visible under normal room lights). In structure A, with PPV closest to the magnesium contact, only green PPV emission is observed. The lack of nanocrystal emission indicates that charge recombination is occurring primarily in the PPV layer. PPV is known to be a poor transport material for electrons, so when it is next to the electron injector in a sandwich configuration the electrons are effectively 'trapped' in the PPV. This puts the recombination zone for electrons and holes in the PPV and close to the metal electrode. A similar phenomenon has been observed in pure polymer bilayer devices that preferentially exhibit emission from the layer closest to the electron injector[13]. The electrical characteristics of structure A samples are quite similar to PPV alone, with operating voltages of ~7 V and standard diode current–voltage (I/V) behaviour (Fig. 2, top).

Drastically different electro-optic properties are observed if the spatial positions of the nanocrystals and the PPV are reversed, giving structure B (Fig. 2, bottom). Under a forward bias of only 4 V, these samples exhibit an emission characteristic of the nanocrystals. Because the operating voltages of these devices are lower than those of PPV alone, we propose that the electron affinity of the nanocrystals must be greater than that of PPV. Not only does a higher electron affinity decrease the 'turn-on voltage' (that is, the voltage at which charge is injected), but it also leads to a situation in which the electrons traversing the CdSe multilayer are more likely to face a barrier at the PPV/CdSe interface leading to a build-up of negative charge there. As observed for heterojunctions[13,14] in multilayer polymer structures, confined carriers help the electroluminescent process both by bringing the recombination zone away from the electrodes (where quenching may occur) and by creating large electric fields at the heterojunction which enhance tunnelling of the electrons into the PPV and holes into the CdSe. The excitons thus formed can diffuse preferentially into the lower-band-gap material giving rise to an emission colour characteristic of recombination in the nanocrystals. Figure 3 clearly shows electroluminescence spectra that shift regularly with nanocrystal diameter (that is, a blue shift with decreasing diameter), thus showing evidence of the quantum confinement effect in nanocrystal electroluminescence.

Whereas most single and bilayer devices fabricated from polymers have been shown to have field dependent I/V characteristics[11,13] (and therefore tunnelling-based charge injection mechanisms), we find that our samples with varying PPV and CdSe multilayer thicknesses have the same I/V characteristics and therefore proceed by a voltage dependent current injection mechanism. This behaviour suggests that the I/V characteristics are determined by charge (in this case electron) injection at the Mg/CdSe interface rather than the ITO/PPV interface. In addition, the voltage dependence of the I/V characteristics suggests our devices have a different majority carrier injection mechanism as compared to the polymer-only devices. Theories involving thermionic emission or a space charge build-up could explain this voltage dependence. We note that these nanocrystal samples have efficiencies 3–10 times larger than those observed in structure A. External quantum efficiencies for both samples, as well as for samples we prepared from PPV alone, are low (0.001–0.01%). However, given that these diodes are unoptimized, there is no reason to believe that these efficiencies are an upper limit. The behaviour of the samples under reverse bias is difficult to measure because sample breakdown occurs readily in this direction. As in single-layer PPV samples,

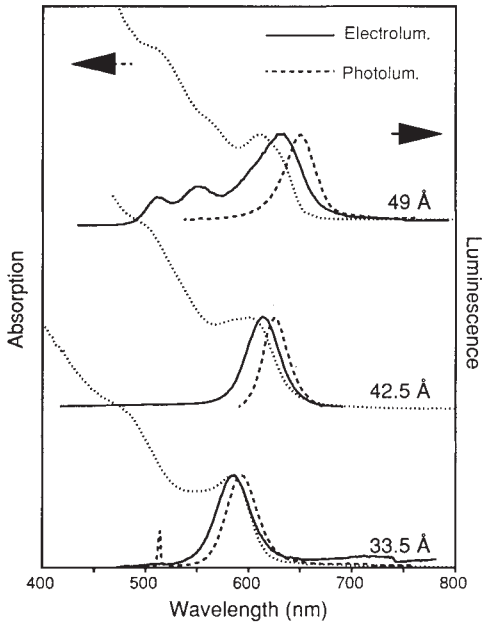

FIG. 3 The quantum confinement effect in the electroluminescence (solid line), photoluminescence (dashed line) and absorption (dotted line) for nanocrystals of three different diameters. The blue shift of the (49, 42.5 and 33.5 Å) electroluminescence with respect to the photoluminescence may be due to trap filling by carriers injected into the CdSe multilayer or to the charge transport mechanism in the CdSe multilayer. The photoluminescence and absorption spectra were taken of nanocrystals dissolved in liquid toluene, whereas the electroluminescence spectra were obtained from our bilayer diode devices. The peak in the photoluminescence spectra at 514 nm is the excitation laser line. The two broad humps (at 515 and 550 nm) in the electroluminescence spectra for the 49 Å sample represent a small amount of emission from the PPV layer, which becomes visible in systems having a thin CdSe layer.

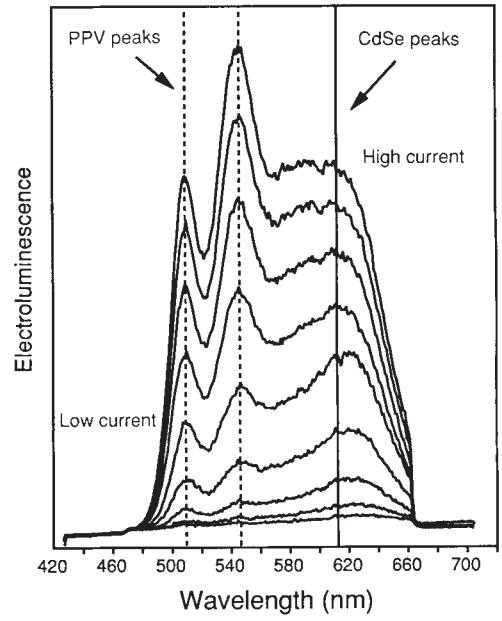

FIG. 4 Voltage-dependent colour of CdSe/PPV samples. In samples with a very thin CdSe layer (one or two monolayers) it is possible to see significant PPV signal in addition to the CdSe signal. At lower voltages CdSe emission dominates, giving a sample with (in this case) a yellow colour. As the voltage is increased the PPV emission becomes more intense, leading to distinctly green luminescence. This phenomenon is completely reproducible over many scans; however, if the sample is kept at bias for >10 min the signal from the PPV will begin to decrease relative to that from the CdSe.

rectification ratios are low and electroluminescence is never observed in reverse bias[15,16].

Another interesting aspect of these samples is their voltage-dependent colour (Fig. 4). At lower voltages, emission occurs preferentially in the CdSe layer, whereas at higher voltages the green-coloured PPV layer dominates. Such a phenomenon has never been observed in bilayer structures of organic polymers, even when similar carrier confinement properties are reported. This behaviour is probably a result of the fact that PPV and CdSe nanocrystals are drastically different materials with disparate dielectric constants and transport mechanisms. If the forms of the field dependences of either charge migration or exciton diffusion are different in the two materials, then the recombination zone could spatially move with voltage. It is also possible that the nanocrystals are behaving as typical bulk inorganic diodes, with falling emission intensities at high currents due to heating of the sample[17]. Voltage tunability of electroluminescence colour has also been observed in electrochemical cells containing porous silicon[1], but in that case there is a continuous shift in emission colour, the origin of which is not known although it may be related to the presence of silicon 'wires' of different diameter in the sample[18]. Our system, in contrast, obtains colour variability from the presence of materials with different emission characteristics. Using this principle, one can envisage creating a multi-colour pixel in which the voltage applied dictates the diode colour. We note that in addition to the voltage dependence of their electroluminescence, the two materials also exhibit different stabilities. If the samples are left under positive bias in air for >10 min, the overall efficiency drops. Although both the PPV and the CdSe peaks shrink with time, the PPV emission disappears altogether, eventually resulting in only nanocrystal emission.

The generation of a light-emitting diode based on an organic/inorganic nanocrystal composite structure built up by assembly of the individual components is a new approach to this technology. Many of the traditional advantages of bulk inorganic semiconductor diodes, namely thermal, chemical and mechanical stability, low operating voltages and high efficiencies can be realized with a material capable of many different emission colours. Moreover, by capitalizing on the established advantages of the organic polymers, such as efficient hole transport and high breakdown voltages, these heterostructures can easily be made large area. Finally, the ability to continuously tune the electron affinity and band gap of the emitting nanocrystal layer by altering the particle size[19-24] provides a powerful tool for elucidating the role of the heterojunction in the process of electroluminescence. □

Received 17 February; accepted 13 June 1994.

1. Bsiesy, A. *et al. Phys. Rev. Lett.* **71,** 637–640 (1993).
2. Burroughes, J. H. *et al. Nature* **347,** 539–541 (1990).
3. Greenham, N. C., Moratti, S. C., Bradley, D. D. C., Holmes, A. B. & Friend, R. H. *Nature* **365,** 628–630 (1993).
4. Steigerwald, M. L. *et al. J. Am. chem. Soc.* **110,** 3046–3050 (1988).
5. Murray, C. B., Norris, D. B. & Bawendi, M. G. *J. Am. chem. Soc.* **115,** 8706 (1993).
6. Bowen Katari, J. E., Colvin, V. L. & Alivisatos, A. P. *J. phys. Chem.* **98,** 4109 (1994).
7. Bradley, D. D. C. *Synthetic Metals* **54,** 401–415 (1993).
8. Burn, P. L. *et al. Nature* **356,** 47–49 (1992).
9. Karg, S., Riess, W., Dyakonov, V. & Schwoerer, M. *Synthetic Metals* **54,** 427–433 (1993).
10. Zhang, C., Braun, D. & Heeger, A. J. *J. appl. Phys.* **73,** 5177–5180 (1993).
11. Parker, I. D. *J. appl. Phys.* **75,** 1656 (1994).
12. Colvin, V. L., Goldstein, A. N. & Alivisatos, A. P. *J. Am. chem. Soc.* **114,** 5221–5230 (1992).
13. Brown, A. R. *et al. Chem. Phys. Lett.* **200,** 46–54 (1992).
14. Brown, A. R. *et al. Appl. Phys. Lett.* **61,** 2793–2795 (1992).
15. Valeeva, I. L. & Lachinov, A. N. *Synthetic Metals* **55–57,** 4151–4156 (1993).
16. Karg, S. *Synthetic Metals* **57,** 4186–4191 (1993).
17. Quist, T. M. *et al. Appl. Phys. Lett.* **1,** 91–93 (1961).
18. Canham, L. *Nature* **365,** 695 (1994).
19. Rossetti, R., Hull, R., Gibson, J. M. & Brus, L. E. *J. chem. Phys.* **82,** 552–559 (1985).
20. Bawendi, M. G., Carroll, P. J., Wilson, W. L. & Brus, L. E. *J. chem. Phys.* **96,** 946–954 (1992).

21. Brus, L. *J. phys. Chem.* **90,** 2555–2560 (1986).
22. Ekimov, A. I. *et al. J. opt. Soc.* **B10,** 100–107 (1992).
23. Dannhauser, T., O'Neil, M., Johannson, K., Whitten, D. & McLendon, G. *J. phys. Chem.* **90,** 6074–6076 (1986).
24. Hasselbarth, A., Eychmuller, A. & Weller, H. *Chem. Phys. Lett.* **203,** 271–276 (1993).
25. Sze, S. M. *Physics of Semiconductor Devices* (Wiley, New York, 1981).
26. Colvin, V. L., Alivisatos, A. P. & Tobin, J. G. *Phys. Rev. Lett.* **66,** 2786–2789 (1991).

ACKNOWLEDGEMENTS. We thank D. Botkin and members of the Chemla group for use of their semiconductor parameter analyser. This work was supported by the US Department of Energy.

Moisture supply for northern ice-sheet growth during the Last Glacial Maximum

Dierk Hebbeln*, Trond Dokken†, Espen S. Andersen‡, Morten Hald† & Anders Elverhøi†‡

* Fachbereich Geowissenschaften, Universität Bremen, Postfach 330440, D-28334 Bremen, Germany
† Institutt for Biologi og Geologi, Universitet Tromsø, N-9037, Norway
‡ Institutt for Geologi, Universitet Oslo, Postboks 1047 Blindern, N-0316 Oslo 3, Norway

During the last ice age, the Barents Sea ice sheet began to grow 22 kyr ago[1], only 8 kyr before it began to disintegrate[2]. This implies that the ice must have grown very rapidly from the coast to the edge of the continental shelf. Such rapid growth of a large ice sheet requires significant amounts of moisture[3], but the origin of this moisture has been unclear, particularly as the CLIMAP climate reconstruction suggests[4,5] that the Greenland–Iceland–Norwegian (GIN) seas were perennially ice-covered during this period. Here we present data from deep-sea sediment cores from the Fram Strait, which suggest that relatively warm water from the North Atlantic Ocean was advected into the GIN seas in two short-term events (27–22.5 and 19.5–14.5 kyr ago). We suggest that the resulting seasonally ice-free waters were an important regional moisture source for the Barents Sea ice sheet, and that the GIN seas played a much more active role in climate during the last glaciation than has previously been supposed.

Today the Norwegian Sea and the eastern Fram Strait are dominated by the Norwegian current and the Westspitsbergen current which transport warm, Atlantic water from the south to the Arctic Ocean (Fig. 1). This circulation pattern has existed for the past 10 kyr since its re-establishment following the glacial–interglacial transition[6]. In the west, the East Greenland current transports cold, polar water and sea ice from the Arctic Ocean to the south. A comparable circulation pattern probably also existed during the last interglacial (130 kyr ago[5,7]). A weak influx of Atlantic water to the GIN seas is also recognized during oxygen isotope substage 5a (~77 kyr ago)[5,7]. In previous reconstructions, isotope stages 4 to 2 were assumed to be characterized by perennial sea-ice cover and by an isolated cold circulation cell in the GIN seas[4,5] (Fig. 1). More recently, the CLIMAP reconstructions of the Last Glacial Maximum (LGM)[4] have been challenged by indications of seasonal ice-free conditions in the southern Norwegian Sea[7–9].

According to our data from the continental slope and deep sea west of Svalbard (Fig. 1), Atlantic water reached the northern GIN seas during isotope stages 3 and 2. Advection of Atlantic water to the Fram Strait is assumed to have started ~27 kyr ago, as documented in the sediments by high amounts of planktonic foraminifera and coccoliths and, therefore, by a relatively high carbonate content (Fig. 2). Because coccoliths are phytoplankton and therefore require light, the presence of coccoliths in sediments from the Fram Strait and Norwegian Sea is interpreted as an indication of seasonally ice-free waters[10].

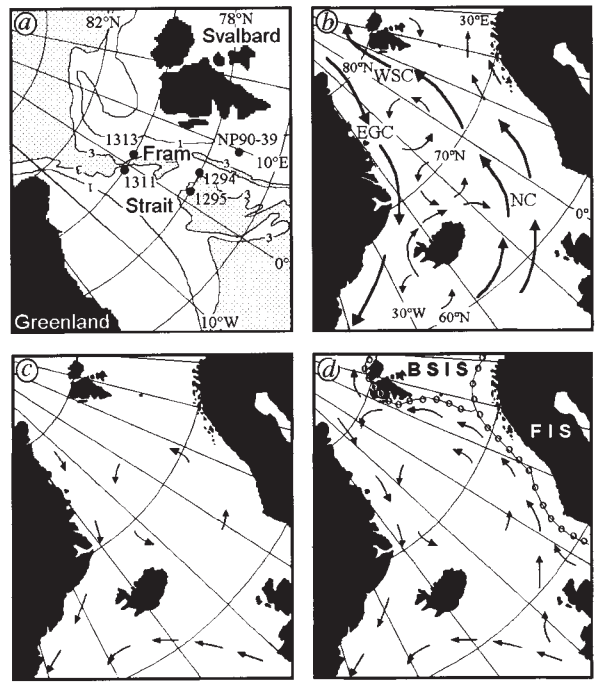

FIG. 1 *a*, Sites of the investigated cores (NP90–39; 77° 15.5′ N, 9° 05.6′ E, 2,119 m: 1294-4; 77° 59.9′ N, 5° 22.3′ E, 2,668 m: 1295-5; 77° 59.2′ N, 2° 24.8′ E, 3,112 m: 1311-4; 79° 57.8′ N, 0° 10.4′ E, 2,615 m: 1313-4; 79° 59.9′ N, 2° 44.8′ E, 2,627 m) and bathymetry of the Fram Strait. 1,000 m and the 3,000 m isobaths are shown with the areas deeper than 3,000 m stippled. *b*, Present-day surface water oceanography of the Greenland–Iceland–Norwegian seas[34]. *c*, Reconstruction of the surface-water circulation for the Last Glacial Maximum (LGM) according to ref. 5. *d*, Reconstruction of the surface-water circulation for the LGM (19.5–14.5 kyr) and for the period 27–22.5 kyr according to this study. The dotted line indicates the extension of the Barents Sea ice sheet (BSIS) and the Fennoscandian ice sheet (FIS) during the LGM[25]. (WSC, Westspitsbergen Current; EGC, East Greenland Current, NC, Norwegian Current).

Most glacial sediments in the GIN seas are totally devoid of coccoliths[10–12]. High numbers of planktonic foraminifera per gram of sediment can be interpreted as reflecting increased surface water productivity and, therefore, point also to seasonally open waters[5]. The species composition of planktonic foraminifera in these high latitudes is clearly dominated by the polar species *Neogloboquadrina pachyderma* (*sin.*)[13]. In the GIN seas high abundances of the subpolar planktonic foraminifer *Globigerina quinqueloba* are characteristic of the oceanic frontal zones (the polar front, dividing polar and Arctic waters, and the Arctic front, dividing Arctic and Atlantic waters[9]). Therefore, the occurence of *Globigerina quinqueloba* in core NP9039 (Fig. 2) indicates the advance of the polar front, or possibly the Arctic front, to the Fram Strait during this interval, resulting in at least seasonally open waters.

From the sediment cores it is evident that the open-water conditions are followed by intensified input of terrigenous material. At ~22.5 kyr ago the ice sheet seems to have expanded into the ocean (Fig. 3), where it could directly affect circulation and sedimentation in the GIN seas. Increased input of terrestrial material is evident in several ways. First, the 0.5–1.5% increase in total organic carbon (TOC) content is paralleled by high C/N ratios (here taken to be the ratio of organic carbon (C_{org}) to total nitrogen) and light $\delta^{13}C_{org}$ values (Fig. 2), which are clear indicators of a terrigenous origin for the organic matter[14] as has been shown also for the GIN seas[15–17]. Second, in core NP90-39 from the Svalbard continental slope (Fig. 1) at ~21 kyr ago, there is a significant increase in ice-rafted detritus (IRD) or